Perkins et al., 2017, Control of landslide volume and hazard by glacial stratigraphic architecture, northwest Washington State, USA: Geology, https://doi.org/10.1130/G39691.1.

SUPPLEMENTARY METHODS

Landslide volume, area, and relative mobility calculations

We use available lidar data (www.dnr.wa.gov/lidar) to calculate mapped landslide volumes with an average end-area method. Total landslide volume is equal to the sum of the volumes of individual segments across a deposit. Segments are defined between two parallel cross sections (e.g., Fig. S1), and segment volumes are approximated as the average cross-sectional area of the two bounding slices multiplied by the distance between them.

We calculate the areas of each cross-sectional slice by estimating the thickness of the deposit at each node along the cross-section profile, then multiplying by the node spacing. Calculating landslide thickness along a cross-section requires knowledge of the deposit base elevation, and we use a variety of methods to estimate landslide basal elevations. For latitudinal cross sections along smoothly varying topography, slide margins are identified along each cross section and the valley floor is linearly interpolated between slide margin elevations. Where deposits are within a drainage network, we project valley fills down to the channel thalweg. This assumption may represent an underestimate of landslide volume if the channel has not fully incised to the slide base and landslide debris may have been removed by post-emplacement fluvial erosion. However, as shown for the case of the Oso landslide, channels can incise through landslide deposits on the order of months. For the four small landslides measured along the North Fork Stillaguamish River (NFSR; Fig. 1 in the main text), we use longitudinal rather than latitudinal cross sections, and estimate deposit depth by projecting the upper failure plane escarpment down to the deposit base at the landslide

toe. For Skagit Valley landslides we measure cross sections every 50 to 100 m, and for Cedar River landslides that have a simpler geometry, we measure sections at larger intervals depending on the complexity of the slide segment (Fig. S1a and b). We also include in our analysis landslide volume measurements from Iverson et al. (2015) and Badger (2015), who calculated landslide volumes along the NFSR using analogous methods. Landslide inundation areas are calculated from landslide boundaries mapped in ArcGIS using lidar data.

Volumes, inundation areas, and UTM coordinates for each slide are compiled in Table S1, and are shown graphically in Figure 1e. Figure 1e also shows an empirical relationship for landslide volume (V) and inundation area (A) that comes from a global compilation of rock avalanche and debris-flow data (Griswold and Iverson, 2008): $A=20V^{2/3}$. Small-volume slides from the NFSR plot well below this empirical relationship, indicating low relative mobility. As these slides failed from the uppermost section of the hillslope onto back-rotated benches created by previous large-volume failures (Fig. 1a), there is less room for the landslides to spread than if they failed onto a flat surface. Across all volumes, landslides along the Cedar terrace have large inundation areas compared to both the empirical relationship and to similar-sized failures along the Skagit valley (Fig. 1e). Given their relatively large inundation areas as well as their morphologic similarity to debris-flows (Fig. 1a and d; Fig. S1b), it is likely the Cedar landslides traveled relatively quickly and therefore represent a relatively high hazard. Large-volume landslides along the NFSR plot relatively close to the statistically expected values, with the exception of the BA6S landslide of Badger (2015), which has about half the expected inundation area (second-largest landslide on Fig. 1e; Table S1). Badger

(2015) notes that this slide has been eroded, possibly significantly, so the measured deposit volume and area therefore represent minimum estimates. Given that a large portion of the inundation area from the similarly shaped Oso (SR 530) landslide exists where the deposit is quite thin, it is not surprising that post-depositional erosion would reduce inundation area of the BA6S landslide much more than overall deposit volume.

Slope stability modeling

Geomorphic approaches to assessing landslide potential within a landscape often rely on one-dimensional infinite slope models (e.g., Montgomery and Dietrich, 1994) that, while instructive for shallow translational landslides, are not appropriate for assessing deep-seated slope failures in which the failure surface is not parallel with the topographic surface. Schmidt and Montgomery (1995) assessed glacial terrace stability using two-dimensional (2D) limit-equilibrium methods; however, their approach is limited to homogeneous material properties. 2D finite element modeling can account for layering differences and groundwater effects found within glacial terraces (e.g., Savage et al., 2000), but this approach cannot resolve landslide volumes directly. Brien and Reid (2008) highlight the efficacy of pairing three-dimensional (3D) slope-stability and groundwater models to examine slope failure style and size in glacial bluffs near Seattle, WA.

Here we follow a methodology similar to that presented by Brien and Reid (2008) and pair a 3D slope-stability model, Scoops3D (Reid et al., 2015), with a 2D variably saturated groundwater model. Although Brien and Reid (2008) use a 3D groundwater model in their analysis of Seattle's topography, to maintain simplicity with our schematic terrace representations we rely on a 2D variably saturated groundwater model (VS2Dt,

described in the next section). Because our model domains are symmetric along the length of the terrace bench, we translate our 2D cross-sectional groundwater model results into 3D by extending the results along the length of the 3D domain. For all cases we use an idealized terrace domain that represents a symmetric bench with similar relief and surface slope to our three study areas (Fig. S2), and create three generalized stratigraphic configurations based on the observed geology of the Cedar, Skagit, and North Fork Stillaguamish terraces respectively.

Scoops3D calculates moment-equilibriums for masses above thousands to millions of potential landslide failure surfaces within a topographic dataset, and can therefore provide factor of safety (*F)* distributions both in the subsurface and throughout a landscape. *F* is defined as the ratio of the driving shear stress on a failure surface, τ, and the resisting shear strength, *s*:

$$\boldsymbol{F} = \frac{\boldsymbol{s}}{\boldsymbol{\tau}} \qquad (1).$$

When the driving stress exceeds the shear strength of the material, *F* becomes less than 1 and failure is expected. Driving moments are calculated from the integrated weight of each overlying column, and resisting moments depend on the shear strength, *s*, which is defined by the Coulomb-Terzaghi equation:

$$s = c + (\sigma_n - u)tan\phi \qquad (2).$$

As shown by Terzaghi (1943), *s* depends upon the effective stress, defined as the normal stress σ_n minus the pore-water pressure *u*, acting on the failure surface. Shear strength is also a function of material cohesion, *c*, and the angle of internal friction, ϕ, both of which can vary considerably in glacial sediments of the Puget Lowlands (e.g., Savage et al., 2000a and b). Values used in our slope-stability analyses and their respective data sources

are shown in Tables S2 and S3. We compute stability values (F) for both dry conditions ($u = 0$), as well as steady-state infiltration conditions where u is determined at all locations in the model domain from groundwater simulations that we describe below. Also, as we model idealized 2D topographic configurations, our results do not consider complexities arising from 3D topographic stresses or hydrologic flow convergence or divergence. In our stability analysis we ignore the effects of unsaturated matric suctions and only assess the destabilizing effects from positive pore pressures. Further explanation of the algorithms used to calculate equilibrium moments can be found in Reid et al. (2015).

Variably saturated groundwater flow modeling

Spatial variability in pore-water pressures within a hillslope can significantly alter the pattern of slope stability, and factor of safety measurements that incorporate these effects will differ markedly from fully saturated groundwater model predictions (e.g., Rulon and Freeze, 1985). To model gravitationally driven groundwater flow through our idealized glacial terraces, we use the USGS program, VS2Dt (Lapalla et al., 1987). VS2Dt solves a 2D form of Richards' equation using van Genuchten functions to describe the nonlinear relationship between hydraulic conductivity, moisture content, and pressure head for different soil properties (Lapalla et al., 1987, van Genuchten, 1980). Saturated hydraulic conductivities and unsaturated van Genuchten parameters used in our analysis are shown in Table S2.

We use boundary conditions for our model similar to other boundary value problems dealing with exfiltration of water from perched aquifers within a hillslope (e.g.,

Rulon and Freeze, 1985) (Fig. S3). We apply no-flow boundaries along the back edge of the model domain as well as the base, and set a vertical flux into the terrace equal to an average precipitation value for the region (~1220 mm yr^{-1} = ~3.9 x 10^{-8} m/s) (http://www.wrcc.dri.edu/cgi-bin/cliMAIN.pl?wa0257). Because we impose rainfall along the sloping side of our terrace where hydraulic conductivities can be lower than the rainfall rate, in these regions we set the vertical infiltration rate equal to the conductivity of the less permeable units (Fig. S3). Above stratigraphic contacts we assign a seepage face boundary condition on the hillslopes to allow potential seepage, and at the margin of the floodplain we apply a constant head boundary condition to reflect the presence of a river.

For our model initial conditions, we start with a saturated terrace in order to avoid some of the nonlinear responses that a propagating wetting front may have on establishing a flow regime. Although the simulations in VS2Dt are transient, we run our models for long durations (100-200 years) to obtain a steady-state configuration, which most simulations achieve within a few years. Although this approach simulates typical conditions that may affect the location and size of slope failures, it does not provide direct insight into failure mechanics driven by transient increased rainy periods that may have played a role in the 2014 SR 530 event (Keaton et al., 2014; Henn et al., 2015; Iverson et al., 2015).

REFERENCES

Badger, T.C., 2015, SR 530 MP 35 to 41 Geotechnical Study: Washington State Department of Transportation, 19 p.

Brien, D.L., and Reid, M.E., 2008, Assessing deep-seated landslide susceptibility using 3-D groundwater and slope-stability analyses, southwestern Seattle, Washington: Reviews in Engineering Geology, v. 20, p. 83–101, doi: 10.1130/2008.4020(05).

Carsel, R.F., and Parrish, R.S., 1988, Developing joint probability distributions of soil water retention characteristics: Water Resources Research, v. 24, p. 755–769, doi: 10.1029/WR024i005p00755.

Henn, B., Cao, Q., Lettenmaier, D.P., Magirl, C.S., Mass, C., Bower, J.B., St Laurent, M., Mao, Y.X., and Perica, S., 2015, Hydroclimatic Conditions Preceding the March 2014 Oso Landslide: Journal of Hydrometeorology, v. 16, p. 1243–1249, doi: 10.1175/jhm-d-15-0008.1.

Iverson, R.M., George, D.L., Allstadt, K., Reid, M.E., Collins, B.D., Vallance, J.W., Schilling, S.P., Godt, J.W., Cannon, C.M., Magirl, C.S., Baum, R.L., Coe, J.A., Schulz, W.H., and Bower, J.B., 2015, Landslide mobility and hazards: Implications of the 2014 Oso disaster: Earth and Planetary Science Letters, v. 412, p. 197–208, doi: 10.1016/j.epsl.2014.12.020.

Keaton, J.K., Wartman, J., Anderson, S., Benoît, J., deLaChapelle, J., Gilbert, R., and Montgomery, D.R., 2014, The 22 March 2014 Oso Landslide, Snohomish County, Washington: Geotechnical Extreme Events Reconnaissance Association Re- port GEER-036, 186 p., http://www.geerassociation.org/administrator/components/com_geer_reports/geerfiles/GEER_Oso_Landslide_Report.pdf.

Lappala, E.G., Healy, R.W., and Weeks, E.P., 1987, Documentation of Computer Program VS2D to Solve the Equations of Fluid Flow in Variably Saturated Porous Media: USGS Water Resources Investigations Report 83-4099, p. 193.

Miller, D.J., and Sias, J., 1998, Deciphering large landslides: linking hydrological, groundwater and slope stability models through GIS: Hydrological Processes, v. 12, p. 923–941, doi: 10.1002/(SICI)1099-1085(199805)12:6<923::AID-HYP663>3.0.CO;2-3.

Montgomery, D.R., and Dietrich, W.E., 1994, A physically based model for the topographic control on shallow landsliding: Water Resources Research, v. 30, p. 1153–1171, doi: 10.1029/93WR02979.

Reid, M.E., Christian, S.B., and Henderson, S.T., 2015, Scoops3D—Software to analyze 3D slope stability throughout a digital landscape: U.S. Geological Survey Techniques and Methods, book. 14, ch. A1, 218p., doi: https://dx.doi.org/10.3133/tm14A1.

Rulon, J.J., and Freeze, R.A., 1985, Multiple seepage faces on layered slopes and their implications for slope-stability analysis: Canadian Geotechnical Journal, v. 22, p. 347–356, doi: 10.1139/t85-047.

Savage, W.Z., Morrissey, M.M., and Arndt, B.P., 2000a, Finite-element analysis of the Woodway landslide, Washington: U.S. Geological Survey Bulletin 2180, 9 p.

Savage, W.Z., Morrissey, M.M., and Baum, R.L., 2000b, Geotechnical properties for landslide prone Seattle area glacial deposits: U.S. Geological Survey Open-File Report 00-228, 5 p.

Schmidt, K.M., and Montgomery, D.R., 1995, Limits to Relief: Science, v. 270, p. 617–620, doi: 10.1126/science.270.5236.617.

Terzaghi, K., 1943, Theoretical soil mechanics: Géotechnique, p. 510, doi: 10.1016/0167-1987(88)90005-0.

van Genuchten, M.T., 1980, A Closed-form Equation for Predicting the Hydraulic Conductivity of Unsaturated Soils1: Soil Science Society of America Journal, v. 44, p. 892, doi: 10.2136/sssaj1980.03615995004400050002x.

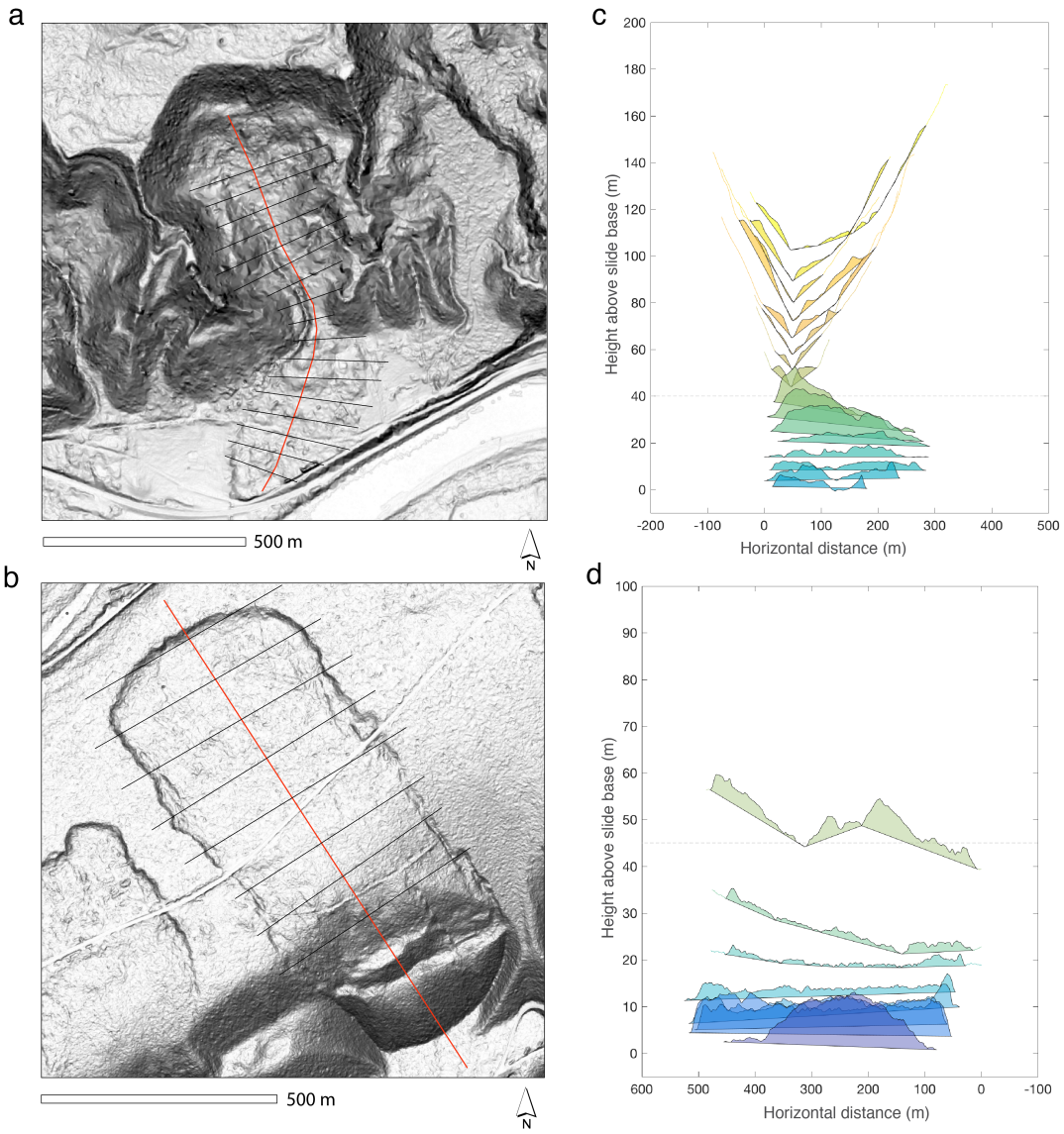

Figure S1. Examples of cross sections through landslides used for volume calculations. (**a**) Locations of latitudinal cross-sections are shown every 50 m along the Skg-1 slide (Table S1). (**b**) Cross sections located every 100 m along the Ced-3 slide. Panels **c** and **d** show cross-sectional areas of each respective landslide deposit. Dashed lines show the elevation of each terrace base, and cooler colors indicate increasing longitudinal distance from the slide headscarp.

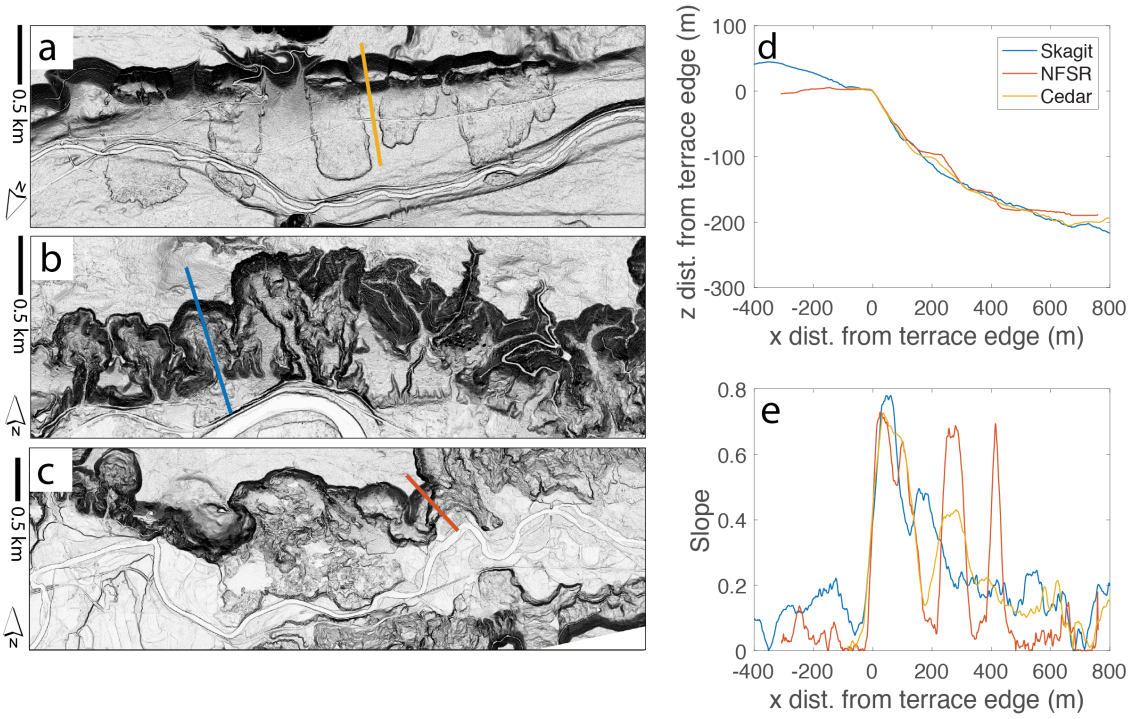

Figure S2. Topographic profiles across the (**a**) Cedar, (**b**) Skagit, and (**c**) North Fork Stillaguamish River glacial terraces. (**d**) Topographic profiles shown as colored lines in **a-c**. Profiles are adjusted so the zero datum corresponds to the upper corner of each terrace. The high elevation mound above the Skagit terrace crest corresponds to a localized subglacial landform. (**e**) Topographic slope for each profile in **d**. Gradients typically peak along the upper slope of each terrace and decline toward their lower boundary. The North Fork Stillaguamish data is taken after the 2006 Hazel landslide but before the 2014 Oso landslide, so Hazel-related scarps show up as similarly steep steps along the profile.

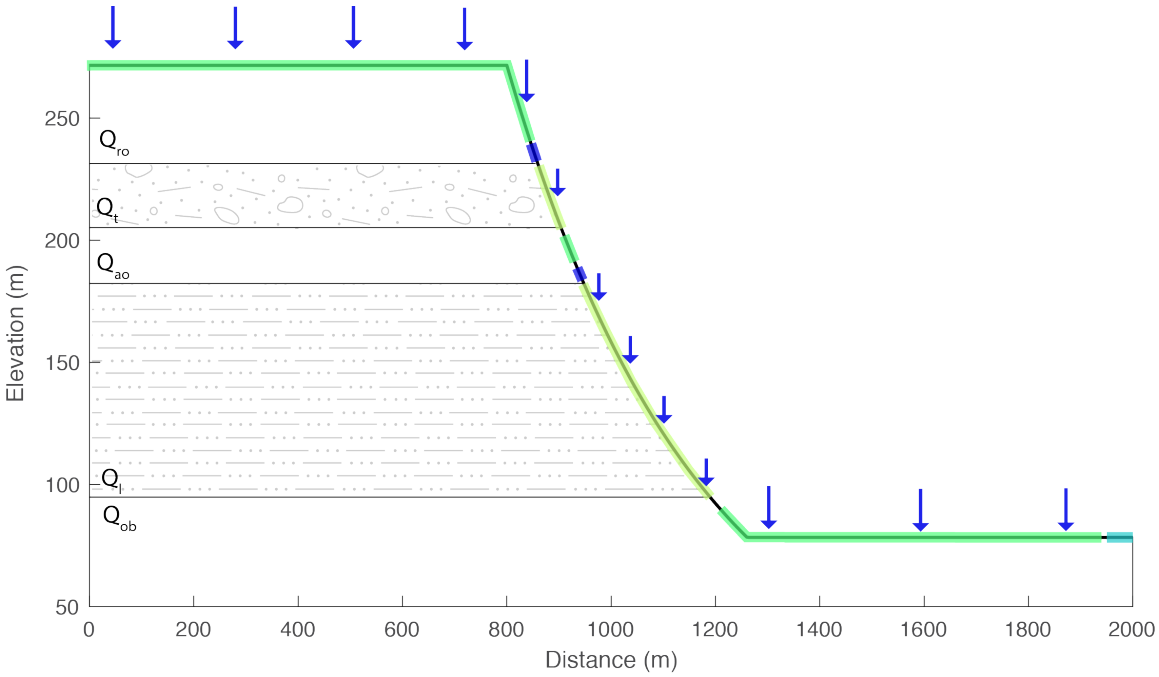

Figure S3. Example of boundary conditions used for VS2Dt simulations. Dark green corresponds to vertical flux equal to an average annual precipitation for the region (~3.9 $x10^{-8}$ m/s). To prevent high pore-fluid pressures along the boundary of the lower-conductivity units from an artificially high flux boundary condition, we set the vertical infiltration equal to the hydraulic conductivity of those units ($1x10^{-9}$ m/s), shown with olive green. Dark blue lines above low-conductivity units are seepage face boundary conditions, and a constant head boundary condition is set for the far right-edge of the floodplain (light blue). Boundary lines without highlighted color represent no-flow boundaries. The domain extends to 0 m depth, but is not shown here.

Landslide	UTM 10N Easting (m)	UTM 10N Northing (m)	Area (m^2)	Volume (m^3)	Method	Comments
Ced-1	590546.35	5251671.351	5.28×10^5	1.73×10^6	lat. slices	
Ced-2	589892.722	5251261.564	3.79×10^5	9.9×10^5	lat. slices	
Ced-3	589140.881	5250833.15	3.27×10^5	9.0×10^5	lat. slices	
Ced-4	588742.947	5250462.309	1.61×10^5	4.5×10^5	lat. slices	
Ced-5	588571.920	5250296.362	4.0×10^4	6×10^4	lat. slices	
Ced-6	588024.972	5250094.855	4.63×10^5	1.21×10^6	lat. slices	
Ced-7	587721.865	5249781.588	8.1×10^4	2.1×10^5	lat. slices	
Skg-1	588220.711	5377699.001	2.11×10^5	9.5×10^5	lat. slices	
Skg-2	587666.143	5377650.318	1.48×10^5	8.9×10^5	lat. slices	
Skg-3	587158.142	5377627.034	1.44×10^5	8.2×10^5	lat. slices	
NFSR-1	583101.943	5348575.934	2.9×10^4	2.6×10^5	lon. slices	
NFSR-2	5840000.470	5348702.934	9×10^3	3×10^4	lon. slices	
NFSR-3	584413.221	5348560.059	1.6×10^4	1.0×10^5	lon. slices	
NFSR-4	584778.346	5348604.509	1.3×10^4	1.3×10^5	lon. slices	
NFSR-Oso	585594.323	5348321.933	1.205×10^6	$8.9 \times 10^{6*}$	lon. slices	*Iverson et al., 2015
NFSR-Rowan	583702.019	5348093.333	2.105×10^6	$3.6 \times 10^{7*}$	lon. slices	*Iverson et al., 2015
NFSR-BA6S	586686.525	5346943.980	6.81×10^5	$2.3 \times 10^{6*}$	unknown	*Badger, 2015 (deposit eroded, minimum est.)

Table S1. Locations and volume-area measurements for landslides in selected sections of the Cedar, Skagit, and North Fork Stillaguamish Rivers.

Layer	Cohesion (kPa)	Internal friction angle (^{o})	Dry unit weight (kN/m^3)	Saturated unit weight (kN/m^3)	Source
Outwash gravels (Q_{ro}/Q_{og})	5*	30	18	20	Savage et al., 2000 *Miller & Sias, 1998
Vashon Till (Q_t)	100	30	21	23	Savage et al., 2000
Advance Outwash (Q_{ao})	10	38	18	20.5*	Brien and Reid, 2008; *Savage et al., 2000
Lawton Clay (Q_l)	29	26	17	19	Brien and Reid, 2008
Olympia Beds (Q_{ob})	19	34	17	20	Brien and Reid, 2008

Table S2. Material property values used for slope-stability modeling.

Layer	Kzz/ Khh	Ss	Saturated Khh (m/s)	Porosity	Residual moisture content	α	β
Outwash/Alluvium (Q_{ro}/Q_{ao}/Q_{og}/Q_{ob})	1	$1x10^{-4}$	$3.6x10^{-6}$	0.39	0.1	5.9	1.48
Clay-rich units (Q_t/Q_l)	1	$1x10^{-4}$	$1x10^{-9}$	0.36	0.07	0.5	1.09

Table S3. Material property values used for groundwater simulations. We use two property classes in our models, one for lower conductivity clay-rich units (Q_t, Q_l) and one for higher conductivity sand and gravel units (Q_{ob}, Q_{ao}, Q_{ro}, Q_{og}). We use default unsaturated material values within VS2Dt for silty clay and sands, which come from Carsel and Parrish (1988). However, we modify the saturated hydraulic conductivity (Khh) for the clay-rich sediments to better reflect values reported in Savage et al. (2000). Ss is specific storage, and α and β are van Genuchten fitting parameters that relate unsaturated hydraulic conductivity and pressure head to moisture content in unsaturated sediments.